Building-Block-Flow Model for Large-Eddy Simulation: Application to the Gaussian Bump

G. Arranz*, Y. Ling† and A. Lozano-Durán‡
Department of Aeronautics and Astronautics, Massachusetts Institute of Technology, Cambridge, MA, 02139

We perform wall-modeled large-eddy simulation (WMLES) of the Gaussian bump using the latest implementation of the Building-block Flow model (BFM) [1, 2]. BFM is a unified subgrid-scale (SGS) and wall model for WMLES that devises the flow as a collection of building blocks. The model is rooted in the assumption that simple canonical flows contain the essential physics to provide accurate predictions in more complex scenarios [3]. BFM is implemented via artificial neural networks and accounts for a limited set of wall-attached turbulence, adverse pressure gradient effects, and separation. The first version of BFM has been already tested on a complex aircraft geometry, showing improvements with respect to standard WMLES approaches [1]. Here, we assess the robustness and capabilities of the second version of BFM in the Gaussian Bump benchmark with emphasis on affordable grid resolutions. The results are compared with available experimental data, as well as results computed using standard WMLES. BFM captures the location and size of the separation bubble with less than 1% error for the coarse grid resolutions considered, improving on standard WMLES approaches. The error in the prediction of the pressure coefficient, friction coefficient, and mean velocities profiles in the second half of the separation bubble is also improved and robust under different grid resolutions. However, the results are still unsatisfactory in the first half of the separation bubble. The mismatch was explained by the lack of training data for BFM to account for strong flow reversal. Future versions of BFM will incorporate additional adverse pressure gradient effects to enhance model performance.

I. Nomenclature

a_∞	=	free-stream sound speed
C_f	=	friction coefficient
C_p	=	pressure coefficient
h	=	half-height of the channel
I_i	=	i-th invariant of the gradient velocity tensor
k	=	correcting factor for ν_t^v
L	=	bump length
M	=	U_∞/a_∞ Mach number
p	=	pressure
Re	=	Reynolds number
$\mathbf{R}$	=	rate-of-rotation tensor
$\mathbf{S}$	=	rate-of-strain tensor
U	=	average streamwise velocity
U_∞	=	free-stream streamwise velocity
$u_\parallel$	=	magnitude of the velocity parallel to the wall
u_t	=	top wall velocity for turbulent Poiseuille-Couette flows
x	=	streamwise coordinate
x_r	=	mean reattachment point at $y/L = 0$
x_s	=	mean separation point at $y/L = 0$

*Postdoctoral Associate, Department of Aeronautics and Astronautics, garranz@mit.edu, and AIAA Member.
†Graduate Student, Department of Aeronautics and Astronautics, lingyn@mit.edu, and AIAA Student Member.
‡Draper Assistant Professor, Department of Aeronautics and Astronautics, adrianld@mit.edu, and AIAA Senior Member.

y	=	vertical coordinate
y_{cv}	=	wall normal distance to a control volume
z	=	spanwise coordinate
Δ	=	characteristic grid resolution
ν	=	kinematic viscosity
ν_t	=	eddy viscosity
ν_t^v	=	eddy viscosity predicted by the Vreman model
ρ	=	fluid density
τ_w	=	shear stress at the wall
DSM	=	Dynamic Smagorinksy model
LES	=	Large-Eddy simulation
RANS	=	Reynolds-averaged Navier-Stokes
SGS	=	Subgrid-scale
WMLES	=	Wall-modelled Large-Eddy simulation
PC	=	turbulent Poiseuille-Couette flow

II. Introduction

Computational fluid dynamics (CFD) has played a key role in the modern aerospace industry for the aerodynamic design of aircraft. However, state-of-the-art CFD models are still unable to comply with the stringent accuracy requirements and computational efficiency demanded by the industry. These limitations are imposed, largely, by the defiant ubiquity of turbulence and the necessity of faithful models able to capture key physical flow phenomena.

An example of a flow topology that evidences the limitations of current CFD methodologies is turbulent boundary-layer separation. Since boundary-layer separation and reattachment can significantly affect the portion of friction drag over an aerodynamic surface [4], accurate prediction of these flow topology remains amongst the most pressing challenges for CFD, as highlighted in the NASA CFD Vision 2030 [5]. To that purpose, a turbulent separated flow validation test case was designed in collaboration between Boeing and the University of Washington. The test consists of a three-dimensional tapered hump or "Gaussian bump", wider in the spanwise direction than the streamwise direction [6]. Owned to its shape, the flow is subjected to a smooth-body separation, whose onset and reattachment points are more challenging to predict than geometrically induced separated flows [7–9].

Numerical simulations of the Gaussian bump with different degrees of fidelity have been already performed. Williams et al. [6] conducted Reynolds-averaged Navier-Stokes (RANS) simulations comparing the pressure coefficient against experimental measurements. They tested the Spallart-Allmaras (SA) turbulence model and the SA model with rotation correction (SARC). In both cases, the models failed to capture the inflection point in the pressure coefficient visible in the experiments. Later, Iyer and Malik [10] performed wall-modeled large eddy simulations (WMLES) of the Gaussian bump. They reported that WMLES is unable to predict flow separation in the mean when medium resolution grids are used. However, the same authors [11] later showed that WMLES is able to capture the separation and reattachment in a fine grid with about 250 Million grid points. In the same vein, Agrawal et al. [7] performed WMLES simulations testing different grid resolutions and subgrid-scale (SGS) models. They showed that some models failed to capture the separation even at the finest grid resolution tested. They also observed a non-monotonic convergence to the solution with grid refinement using standard models, which remains a key challenge of WMLES [12, 13].

The poor performance of current WMLES approaches calls for the exploration of new venues to develop robust and accurate models for wall-model large-eddy simulation. Here, we perform WMLES of the Gaussian bump using the latest implementation of the Building-block Flow model (BFM) [1, 2] with emphasis on coarse grid resolution and consistent monotonic convergence. BFM is a unified SGS and wall model for LES that devises the flow as a collection of building blocks. The core assumption of the model is that simple canonical flows contain the essential physics to provide accurate predictions in more complex flows. It is also envisaged to provide accurate results with coarse resolutions (affordable for industrial applications). This model has been already tested on a complex aircraft geometry showing improvements with respect to standard WMLES [1]. We use the Gaussian bump benchmark to further assess the robustness and capabilities of the BFM. The results are compared with available experimental data and standard WMLES models.

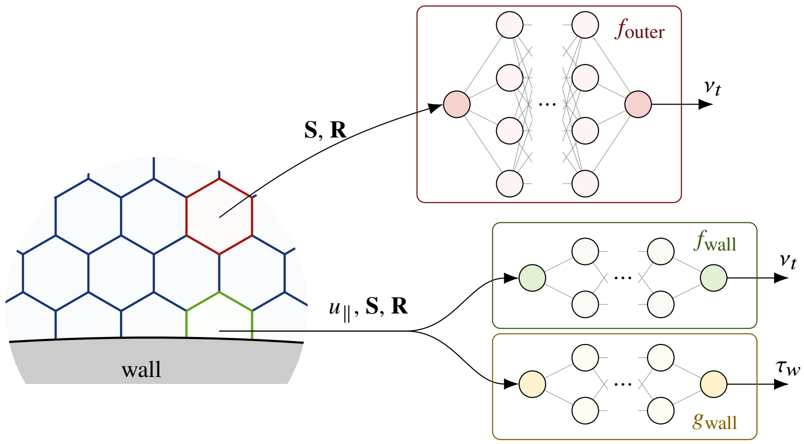

Fig. 1 Schematic of thr building-block flow model (BFM). The panel shows a cross section of a given grid close to a wall. For a control volume that does not touch a wall (red cell) the model computes $\nu_t = f_{\mathrm{outer}}$ from the local instantaneous values of S and R. For a control volume close to the wall (green cell) the model computes $\nu_t = f_{\mathrm{wall}}$ from the local instantaneous values of S, R and $u_{\|}$; and $\tau_w = g_{\mathrm{wall}}$ from the local instantaneous value of $u_{\|}$. Note that the schematics of the ANNs do not depict the actual number of layers and neurons.

III. Methodology

A. Building-block flow model

1. Model architecture

The main modeling hypothesis of the BFM is that the SGS physics of complex flows can be locally mapped into the small scales of simpler canonical flows [3]. Therefore, the BFM is capable of accurately predicting the statistical properties of complex flows as long as the canonical flows used for training are representative of the (missing) SGS flow physics. A detailed discussion about the modeling assumptions of the BFM can be found in Lozano-Durán and Bae [2]. Here, we test the ability of a limited collection of simple turbulent Poiseulle-Coutte flows to model separation in the Gaussian bump.

Figure 1 displays the main components of the BFM. The anisotropic component of the SGS stress is given by the eddy-viscosity model

$$\tau = -2\nu_t \mathbf{S}, \tag{1}$$

where $\mathbf{S}$ is the rate-of-strain tensor and ν_t is the eddy viscosity. The latter is parameterized using artificial neural networks (ANNs) as

$$\nu_t = f_{\mathrm{outer}}(I_1, I_2, I_3, I_4, I_5; \theta), \tag{2}$$

$$\nu_t = f_{\mathrm{wall}}(I_1, I_2, I_3, I_4, I_5, u_{\|}; \theta), \tag{3}$$

where the function f_{wall} computes the eddy-viscosity at the control volumes that are in contact with the wall; and the function f_{outer} computes ν_t at the rest of control volumes in the fluid domain. The inputs for f_{wall} and f_{outer} are five of the invariants of the rate-of-strain and the rate-of-rotation ($\mathbf{R}$) tensors, defined as [14]

$$\begin{aligned} I_1 &= \mathrm{tr}\left(\mathbf{S}^2\right), & I_2 &= \mathrm{tr}\left(\mathbf{R}^2\right), \\ I_3 &= \mathrm{tr}\left(\mathbf{S}^3\right), & I_4 &= \mathrm{tr}\left(\mathbf{S}\mathbf{R}^2\right), \\ I_5 &= \mathrm{tr}\left(\mathbf{S}^2\mathbf{R}^2\right), \end{aligned} \tag{4}$$

together with the magnitude of the velocity parallel to the wall ($u_{\|}$) for f_{wall}. The vector θ contains the variables ν and the characteristic grid size, Δ, that are used for non-dimensionalization, as detailed below.

The model for τ_w is a simplified version of the one presented in Lozano-Durán and Bae [2] and the reader is referred there for more details. The current version does not include a classification and only uses $u_{\|}$, the wall-normal distance

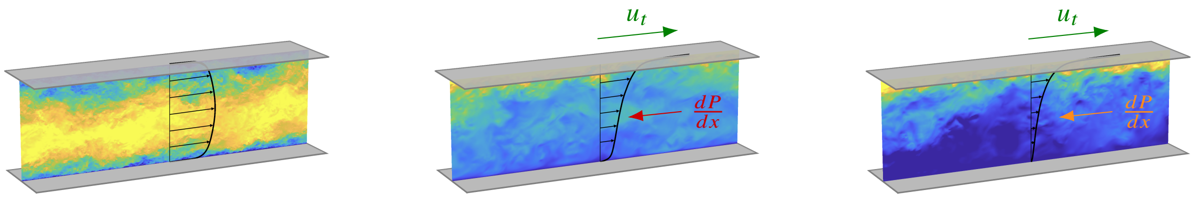

(a) (b) (c)

Fig. 2 Example of building block flows. (a) Turbulent channel flow; (b) turbulent PC flow with a mild pressure gradient (PCm); and (c) turbulent PC flow with a stronger pressure gradient (PCs), leading to flow separation at the bottom wall.

to the control volume (y_{cv}), and $\theta = [\nu, \Delta]$ as inputs

$$\tau_w = g_{\text{wall}}(u_{\|}, y_{cv}; \theta). \tag{5}$$

For the control volumes adjacent to the walls (g_{wall} and f_{wall}), the input and output quantities are non-dimensionalized using viscous scaling (ν and Δ). For the rest of the control volumes (f_{outer}) the input and output variables are non-dimensionalized using semi-viscous scaling ($(\sqrt{I_1}\nu)^{1/2}$ and Δ). The choices above yielded the best performance during the training of the ANNs. Finally, the ANNs are fully-connected feed-forward networks: f_{wall} consists of 8 layers with $[7, 8, 8, 8, 7, 6, 5, 3]$ neurons per each layer; f_{outer} consists of 10 layers with 16 neurons per layer; and g_{wall} consists of 6 layers with 40 neurons per layer.

2. Training data generation

In the present version of the BFM*, we consider two building-block flows: turbulent channel flows, and turbulent Poiseuille-Couette (PC) flows. In both cases, the incompressible flow is confined between two infinite parallel walls separated by a distance $2h$. Figure 2 shows the set-up for both canonical cases. In the turbulent channel flow, the walls are static, and a constant pressure gradient drives the flow in the streamwise direction. In the turbulent PC flow, the bottom wall is static, whereas the top wall moves at a constant speed (u_t) in the parallel direction, and an adverse pressure gradient (dP/dx) is applied in the direction opposite to u_t. For the turbulent channel flows we consider 6 different Reynolds numbers: $Re_\tau = 180, 550, 950, 2,000, 4,200$ and $10,000$, where $Re_\tau = u_\tau h/\nu$ and $u_\tau = \sqrt{\tau_w/\rho}$. For the turbulent PC cases, the pressure gradient ranges from mild to strong, leading to flow reversal on the bottom wall. The PC building-block flows are chosen as representative of separated flows. In particular, three cases are considered: the case with a mild pressure gradient, which features a low positive (i.e., in the same direction as u_t) velocity at the bottom wall; a case with incipient 'separation' ($u \approx 0$ close to the bottom wall); and a case with flow reversal ($u < 0$ close to the bottom wall). They are labeled as PCm, PCs and PCr, respectively, and their Reynolds numbers based on the pressure gradient are $Re_P = \sqrt{h^3 \mathrm{d}P/\mathrm{d}x}/\nu = 340, 680$ and 962. For the three cases, the Reynolds number based on the top wall velocity is $Re_U = u_t h/\nu = 22,360$. Their velocity profile is shown in Fig. 3 for reference.

To generate the data, we perform WMLES simulations of the building blocks adjusting ν_t to match the mean DNS velocity profile. The simulations are performed in charLES, which enables the model to account for the numerical errors of the flow solver. This is the main improvement of the current version of BFM with respect to its predecessor [1]. The eddy viscosity is adjusted by finding a correcting factor k, to the eddy-viscosity predicted by the Vreman SGS model (ν_t^v) [15], namely

$$\nu_t(x, y, z, t) = \nu_t^v(x, y, z, t)k(y) \tag{6}$$

The correcting factor is in turn computed by solving the optimization problem

$$\arg\min_{k(y)} \int |U^{\text{DNS}}(y) - U(y)|^2 dy \tag{7}$$

where U^{DNS} is the mean velocity profile from DNS profile and U is the mean velocity profile computed using the eddy viscosity in Eq. (6). The free Conjugate-Gradient algorithm [16] and the Bayesian Global optimization algorithm

*BFM-v0.2.0

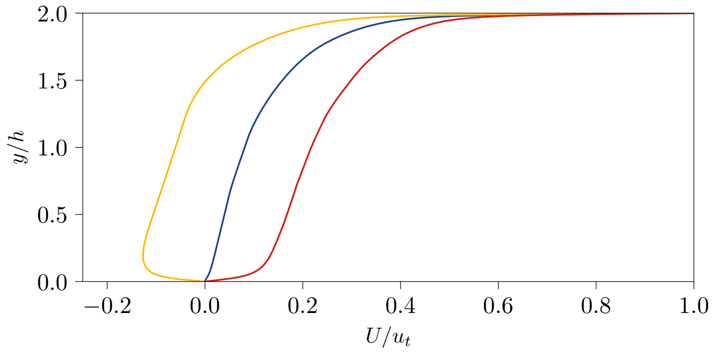

Fig. 3 Average velocity profile of the turbulent PC cases. (red line) PCm; (blue line) PCs; and (yellow line) PCr.

[17, 18] are used to minimize Eq. (7) for the turbulent channel and the turbulent PC flows, respectively. The optimization process for a given case is as follows: 1) an LES simulation is performed with a fixed τ_w –equal to the correct value from DNS simulations, τ_w^{DNS}– and with an initial random $k(y)$; 2) the simulation is run until the statistical steady state is reached; 3) the integral in Eq. (7) is evaluated, and 4) a new guess of $k(y)$ is provided by the optimizer. This approach is continued until the condition

$$\frac{|U^{\mathrm{DNS}}(y) - U(y)|}{U^{\mathrm{DNS}}(y)} < 0.03$$

at each y location for the turbulent channel flow cases is satisfied. For the turbulent PC cases, this condition was too stringent, since velocities are close to 0 near the wall, and we relaxed the condition to

$$\frac{|U^{\mathrm{DNS}}(y) - U(y)|}{u_t} < 0.02.$$

The LES cases to generate the training data were conducted in a computational domain $L_x \times L_y \times L_z = 4\pi h \times 2h \times 2\pi h$, where h is the channel half-height. The time step was chosen to ensure that the Courant–Friedrichs–Lewy number is less than 2. The grid size (Δ) was kept constant for the whole fluid domain (i.e., no near-wall refinement). We performed simulations for $\Delta \approx 0.2h$ and $0.1h$ for the turbulent channel simulations and $\Delta \approx 0.1h$ for the turbulent PC simulations. boundary layer thickness, and are representative of affordable computational meshes for industrial applications.

The mean DNS quantities for the channel flows with Re_τ = 180, 550, 950, 2000 and 4200 corresponds to those from the database by Jimenéz and coworkers [19–21]. The DNS data for the channel flow with $Re_\tau = 10,000$ is obtained from Hoyas et al. [22]. Data for the mean DNS quantities of the turbulent Poiseuille-Couette flows are generated using our in-house code. More details on the *a priori* testing can be found in Ling et al. [1] for the previous version of the model.

B. Case description

The geometry of the bump is given by the analytical formula [6]

$$z(x, y) = \frac{h_0}{2} \exp\left(-\left(\frac{x}{x_0}\right)^2\right)\left[1 + \mathrm{erf}\left(\frac{\frac{L}{2} - 2y_0 - |y|}{y_0}\right)\right], \tag{8}$$

where x, y and z are the streamwise, spanwise and vertical directions, respectively; L is the length of the bump; and the parameters $h_0 = 0.085L$, $x_0 = 0.195L$ and, $z_0 = 0.06L$ define the shape of the bump. Cross-sectional views of the bump in $y/L = 0$ and $x/L = 0$ planes are displayed in Figs. 4a and 4b, respectively.

The non-dimensional parameters that define the flow are the Reynolds number based on the bump length and the free-stream velocity (U_∞), $Re_L = U_\infty L/\nu$, where ν is the free-stream kinematic viscosity; and the Mach number, $M = U_\infty/a_\infty$, where a_∞ is the free-stream speed of sound. The present simulations were performed at $Re_L = 3.4 \cdot 10^6$ and $M = 0.176$. These values are the same as in Williams et al. [6], who reported the pressure coefficient along the centerline; and they are comparable to those in Gray et al. [23], who experimentally computed the friction coefficient and the flow field for $Re_L = 2 \cdot 10^6$ and $M = 0.2$.

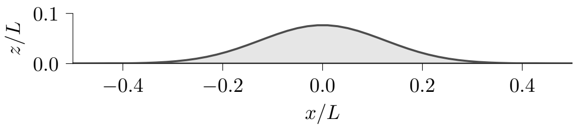

(a)

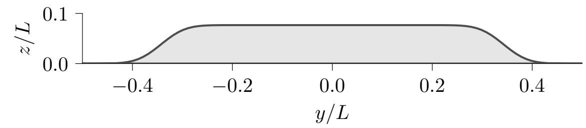

(b)

Fig. 4 Cross-sectional view of the surface defined by Eq. (8). **(a)** $y/L = 0$ **and (b)** $x/L = 0$**.**

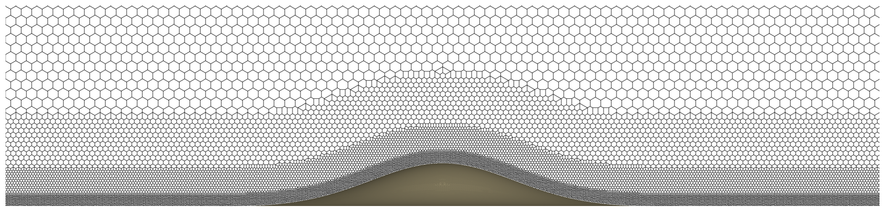

(a)

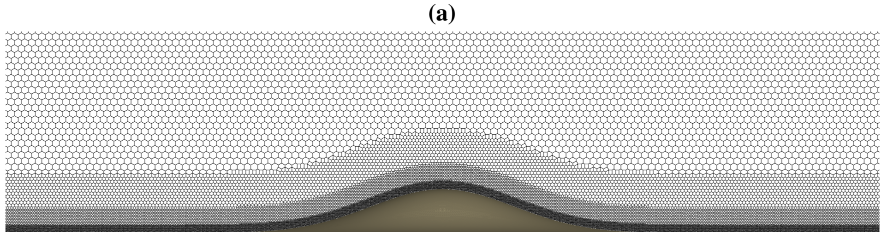

(b)

Fig. 5 Grid structure in the $y/L = 0$ **plane. (a) Extra coarse grid; (b) Coarse grid. Note that the pictures does not include the whole domain in the streamwise direction.**

To assess the performance of the BFM (detailed in § III.A), we compare the results with the predictions obtained using the Dynamic Smagorinksy model (DSM) [24] as the subgrid-scale (SGS) model and the equilibrium wall model (EQWM) [25]. All the simulations were performed using the code charLES from Cascade Tech., Inc. [26]. The solver integrates the filtered Navier-Stokes equations using a skew-symmetric finite volume formulation that has reduced dispersion error and is at least second-order accurate. The numerical discretization relies on a flux formulation that is approximately entropy preserving in the inviscid limit, thereby limiting the amount of numerical dissipation added into the calculation. The time integration is performed with an explicit five-stage third-order strong stability preserving Runge-Kutta method. The mesh generator is based on a Voronoi hexagonal close packed point-seeding method which automatically builds high-quality meshes for arbitrarily complex geometries with minimal user input.

C. Computational set-up

The computational domain is a rectangular prism that extends $\pm 1.5L$ in the streamwise direction, $\pm 0.5L$ in the spanwise direction and from $0L$ to $0.5L$ in the vertical direction. The lateral and top boundaries are free-slip, a constant uniform inflow is imposed at the inlet, and the non-reflecting characteristic boundary condition with constant pressure is applied at the outlet. These boundary conditions are the same as in Iyer and Malik [10] and Agrawal et al. [7].

We consider two grids: a coarse grid, and an extra coarse grid, which are depicted in Figs. 5a and 5b, respectively. Both grids have three levels of isotropic refinement. Each refinement level has roughly 10 control volumes along the wall-normal direction and the average size of each level is twice the size of the previous level. The grid size of the layer closer to the wall is the smallest and is referred to as $\Delta_{\min}$. For the extra coarse grid $\Delta_{\min}/L = 2.2 \cdot 10^{-3}$, and for the coarse grid $\Delta_{\min}/L = 1.4 \cdot 10^{-3}$. The latter is similar to the coarse grid used in Agrawal et al. [7], and from there the name. The grid size and number of elements for each grid are compiled in Table 1. The simulations have been performed with a varying time step to ensure that the Courant–Friedrichs–Lewy number is less than 2.

Mesh	$\Delta_{\min}/L$	N_{cv}
Extra coarse	$2.2 \cdot 10^{-3}$	$8.7 \cdot 10^{6}$
Coarse	$1.4 \cdot 10^{-3}$	$20.3 \cdot 10^{6}$

Table 1 Minimum grid size and number of control volumes, N_{cv}.

IV. Results

We assess the performance of the BFM to predict average quantities of interest in the Gaussian bump. In particular, we examine the average wall pressure and friction coefficients, the location of the separation bubble, and the mean velocity profiles. The results are compared to those from Dynamic Smagorinksy model (DSM) with the equilibrium wall model (EQWM). In the following, we refer to this model as DSM-EQWM-X, where X is the grid: ExtraC(oarse) or C(oarse). All the quantities have been averaged for at least $30U_\infty/L$ convective time units after the initial transient has been discarded.

The average pressure and friction coefficients are computed as

$$C_p = \frac{p - p_\infty}{\frac{1}{2}\rho_\infty U_\infty^2}, \qquad C_f = \frac{\tau_w}{\frac{1}{2}\rho_\infty U_\infty^2},$$

where p_∞ and ρ_∞ are the reference pressure and density, respectively, and p and τ_w are averaged over time. Figure 6a shows the evolution of the pressure coefficient at the centerline ($y/L = 0$). The experiments show a region with a favorable pressure gradient (FPG) before the apex of the bump ($x/L < 0$), followed by a region with an adverse pressure gradient (APG) ($x/L > 0$). Due to flow separation, C_p is not symmetric with respect to the x-axis, but there is an inflection point at $x/L = 0.1$ [6], indicating the mean separation point (x_s). The boundary layer reattaches on average at $x_r/L = 0.36$ [23]. We can observe that all the models predict the evolution of the pressure coefficient in the FPG region regardless of the grid resolution. In the APG region, the DSM-EQWM-ExtraC fails to predict the inflection point, leading to higher values of C_p in the recirculation region compared to the experiments. DSM-EQWM-C captures the inflection point in C_p linked to the onset of separation; however, the pressure inside the separation bubble is overpredicted.

For the BFM, the inflection point is correctly captured for both grid resolutions, but the pressure coefficient is higher than the experimental value. The C_p predicted by the BFM remains constant in the first half of the separation bubble, matching the experimental results in the second half and outperforming the results from DSM-EQWM-C. The C_p predicted by the BFM approaches the experimental results with grid refinement but is less sensitive to changes in the grid resolution than DSM-EQWM.

The prediction of the friction coefficient is shown in Fig. 6b. The experimental values show an abrupt increase of C_f in the FPG region towards the apex of the bump, where the friction coefficient reaches its maximum value. This is followed by a sudden drop in the APG, where $C_f < 0$ in the recirculation region. The trend of C_f in the FPG is consistent for all the models regardless of the grid resolution. Although none of the models is able to match the experimental results in the FPG region, it is interesting to note that BFM underpredicts the wall shear stress. This is expected as the building-blocks used for training BFM do not include cases with favorable pressure gradients. Also, note that the friction coefficient predicted by the DSM-EQWM-ExtraC for $x/L < -1$ is lower than the experimental value and the BFM predictions. This is due to the fact that the flow is laminar for DSM-EQWM-ExtraC for $x/L < -1$, contrary to the flow obtained using BFM for the same grid resolution, which remains turbulent along x.

The mean separation point (x_s) and reattachment point (x_r) are defined as the streamwise locations where $C_f = 0$. For the sake of comparison, Table 2 compiles the mean separation point and mean reattachment point along the centerline for the different cases. DSM-EQWM-ExtraC predicts larger friction coefficients than the experimental results for $x/L > 0$. As a result, the recirculation region is smaller and the onset of separation is delayed. DSM-EQWM-C predict a C_f closer to the experiment results. The prediction of the separation point is improved, and the size of the bubble increases ($0.22L$), although it is still smaller than the experimental bubble ($0.26L$).

The performance of BFM-ExtraC in the APG region is superior to DSM-EQWM-ExtraC. Although the prediction of x_s is identical, BFM-ExtraC captures the exact location of reattachment, improving even upon DSM-EQWM-C. The values of C_f at $x/L > 0.1$ are also closer to the experimental values: the friction coefficient is slightly underpredicted in the first half of the recirculation region, in line with the pressure coefficient; but it matches the experimental values for $x/L \gtrsim 0.23$. By increasing the grid resolution, BFM-C is able to match the exact location for x_s. Therefore, it is likely that the extra coarse grid does not have a sufficient number of control volumes per boundary layer thickness to predict

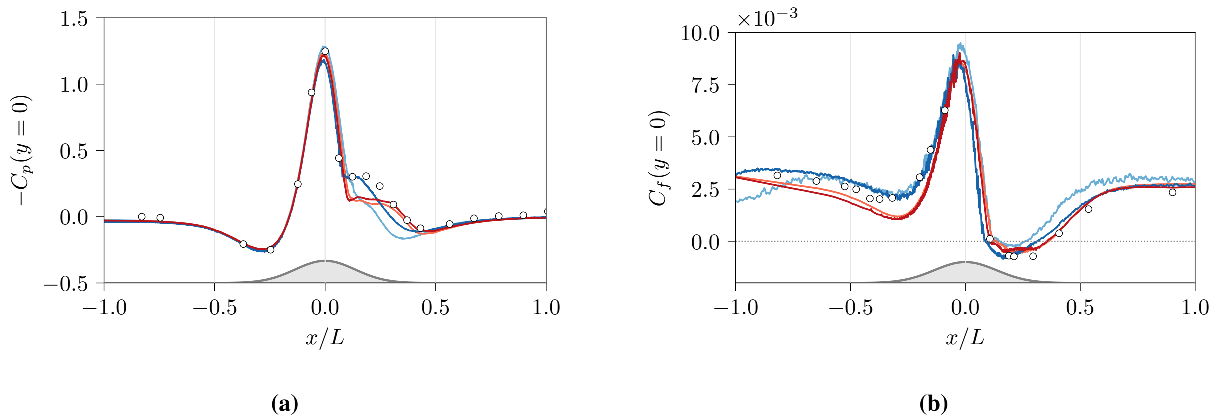

Fig. 6 (a) Average pressure coefficient and (b) average friction coefficient over the bump surface at at $y/L = 0$. Line colors correspond to (light blue) DSM-EQWM-ExtraC; (dark blue) DSM-EQWM-C; (light red) BFM-ExtraC; and (dark red) BFM-C cases. White circles in (a) correspond to experimental results from Williams *et al.* at $Re_L = 3.41 \cdot 10^6$, $M = 0.17$, and (b) experimental results from Gray et al. [23] at $Re_L = 2 \cdot 10^6$, $M = 0.2$.

Case	x_s/L	x_r/L
Gray et al. [23]	0.10	0.36
DSM-EQWM-ExtraC	0.13	0.25
DSM-EQWM-C	0.09	0.31
BFM-ExtraC	0.13	0.36
BFM-C	0.10	0.36

Table 2 Location of mean separation point (x_s) and mean reattachment point (x_r) along the centerline for the different cases

the separation at the exact location. We also note that the prediction of C_f improves by increasing grid resolution, as observed for the pressure coefficient.

Figure 7 displays the average streamwise velocity in the $y/L = 0$ plane for all the cases. The recirculation region corresponds to zones colored in red and yellow. As inferred from C_p and C_f measurements, Fig. 7a shows that the DSM-EQWM-ExtraC predicts a small separation bubble. A quantitative improvement is observed for BFM-ExtraC (Fig. 7b), although the separation bubble is thinner than the one measured experimentally (see Fig. 9 in Gray et al. [23]). Refining the grid improves the prediction of the separation bubble for both models (compare Fig. 7b,d to Fig. 7a,c, respectively). In particular, BFM-C provides the separation bubble that resembles the most to the experimental results in terms of size and shape.

By comparing the recirculation regions in Fig. 7b and 7d, we see that the magnitude of the velocity close to the wall is higher for the DSM-EQWM than for the BFM. Since higher velocities can be linked to a lower pressure and higher (negative) friction coefficients, a likely reason for the smaller values of C_p and C_f predicted BFM may be the underprediction of the velocity magnitude in the region with strong APG. To further support this hypothesis, Fig. 8 depicts the average velocity profile at selected streamwise locations where experimental data is available [23]. Upstream x_s (probe 1), the flow is attached, and all models provides a velocity profile similar to the experimental mean velocity profile. At the beginning of the separation bubble (probe 2), DSM-EQWM-C predicts a reversal flow stronger than the experiments close to the wall, whereas BFM-C predicts a lower velocity, in line with our hypothesis. As the separation bubble further develops downstream (probe 3), all models fail to capture the strong reversal velocity. This is consistent with the higher pressure and lower friction predicted by the models at $x/L \approx 0.23$. At the second half of the separation bubble (probe 4), the magnitude of the negative velocity close to the wall is milder and is accurately captured by the BFM as opposed to DSM-EQWM, which predicts re-attached flow.

From the previous discussion, we can infer that BFM tends to underpredict the velocity in regions with strong flow reversal. The most likely explanation is that the model has not been trained with building-blocks representative of this

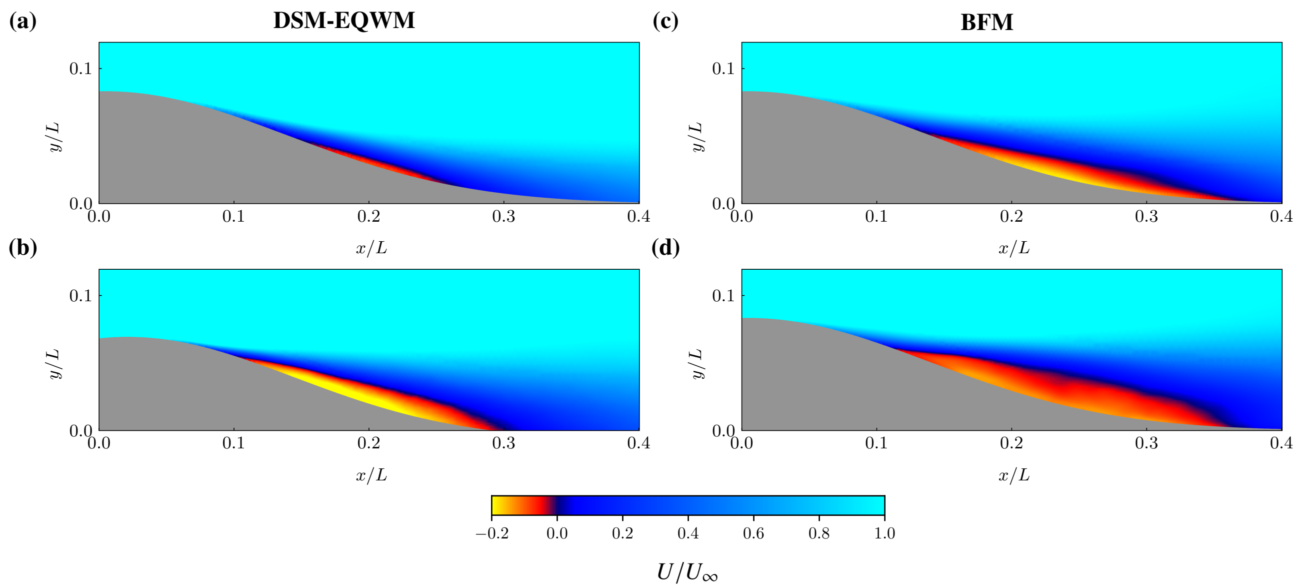

Fig. 7 Average streamwise velocity (U/U_∞) in the $y/L = 0$ plane for different cases: (a) DSM-EQWM-ExtraC; (b) DSM-EQWM-C; (c) BFM-ExtraC; and (d) BFM-C.

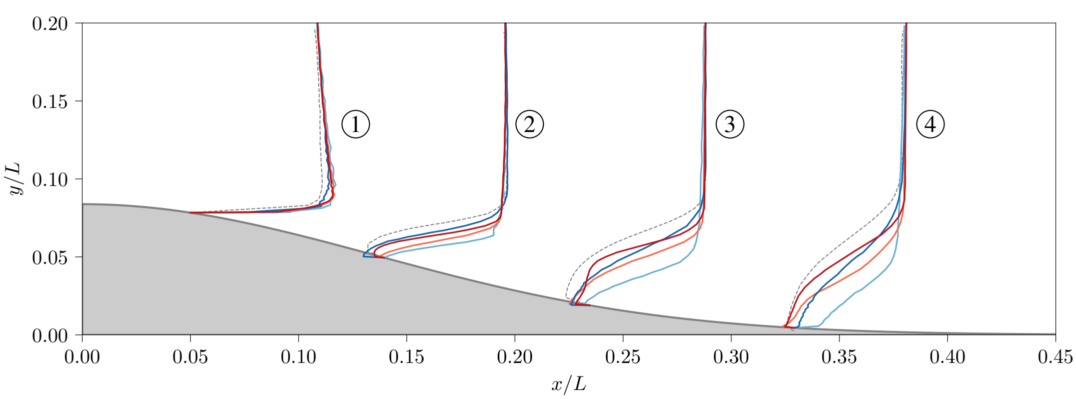

Fig. 8 Average velocity profile at $y/L = 0$ at different streamwise stations. Line colors correspond to (light blue) DSM-EQWM-ExtraC; (dark blue) DSM-EQWM-C; (light red) BFM-ExtraC; and (dark red) BFM-C cases. Dashed lines correspond to the experimental mean velocity profiles from Gray et al. [23]. Note that $U/U_\infty = 0$ is imposed at the surface to show streamwise location of the probe.

case. Namely, among the 9 different blocks used for training, only one case, PCr (Re_P = 962) contains a region with flow reversal. Therefore, two model improvements will be adopted in the future. First, the model will be further trained with PC cases showing stronger reversal flows (i.e., higher Re_P). Secondly, we will add a classification step for the control volumes close to the wall, that will label each control volume as a different type of flow. Depending on the label, different ANNs –trained only with a particular type of flow– will be used to predict ν_t and τ_w. In this manner, the ANNs can be tailored to provide more accurate results. Note that, this additional step was already included in Lozano-Durán and Bae [2] and Ling et al. [1], but it was not implemented in the present work for simplicity. It is anticipated that these modifications will improve the performance of BFM, especially in the separation bubble.

V. Conclusions

We have examined the performance of the latest implementation of the building-block flow model (BFM)[†] for large-eddy simulation. The model is devised to address the challenges faced by CFD in the industry, i.e., the need for accurate and robust solutions at an affordable computational cost. The core assumption of BFM is that the subgrid-scale physics of complex flows can be mapped into the physics of simpler canonical flows [2, 3].

The model consists of an SGS model that computes the eddy viscosity in the flow and a wall model that predicts the wall shear stress. The eddy viscosity and wall shear stress are parameterized using artificial neural networks (ANNs). The training data are generated from LES simulations of the building blocks whose eddy viscosity has been controlled to yield the correct mean velocity profile. The correction step is formulated as an optimization problem and solved by means of a free Conjugate-Gradient method with Bayesian optimization. The training data are generated using coarse grids to ensure the applicability to industrial cases where finer meshes are not affordable. In the current version tested, the model has been trained using a limited set of data from turbulent channel flows at different Re_τ and turbulent Poiseuille-Couette flows with varying adverse pressure gradient.

The performance of BFM was evaluated in the Gaussian bump [6] and the results were compared to the Dynamic Smagorinksy model with the equilibrium wall model (DSM-EQWM). We tested both models in coarse grids, where standard WMLES approaches show difficulties in predicting smooth-body separation [10]. The results show that BFM consistently improves on the prediction of the location and size of the separation bubble when compared to DSM-EQWM simulations. This improvement is particularly noticeable for the coarsest grid tested, where DSM-EQMW predicts almost no separation. Compared to experimental measurements, BFM accurately predicts the pressure and friction in the second half of the separation bubble. However, it yields a higher pressure and lower friction in the first half of the separation bubble. The mismatch was explained by the lower velocities predicted by the SGS model in the regions with a strong flow reversal. To improve model performance, we will continue the training of the model with additional cases accounting for adverse pressure gradient effects. A classifier will be also added to label the type of flow for the control volumes close to the wall, enabling the use of tailored ANNs.

Acknowledgments

The authors acknowledge the Massachusetts Institute of Technology, SuperCloud, and Lincoln Laboratory Supercomputing Center for providing HPC resources that have contributed to the research results reported here. G. A. was partially supported by STTR grant no. N68335-21-C-0270 NAVAIR - Cascade Technologies.

References

[1] Ling, Y., Arranz., G., Williams., E., Goc, K., Griffin, K., and Lozano-Durán, A., "WMLES based on building block flows," *Proceedings of the Summer Program, Center for Turbulence Research , Stanford University*, 2022.

[2] Lozano-Durán, A., and Bae, H. J., "Machine-learning building-block-flow wall model for large-eddy simulation," , 2023.

[3] Lozano-Durán, A., and Bae, H. J., "Self-critical machine-learning wall-modeled LES for external aerodynamics," *Center for Turbulence Research - Annual Research Briefs*, 2020, pp. 197–210.

[4] Simpson, R. L., "Aspects of turbulent boundary-layer separation," *Prog. Aerosp. Sci.*, Vol. 32, No. 5, 1996, pp. 457–521. https://doi.org/10.1016/0376-0421(95)00012-7.

[†]BFM-v0.2.0

[5] Slotnick, J., Khodadoust, A., Alonso, J., Darmofal, D., Gropp, W., Lurie, E., and Mavriplis, D., "CFD Vision 2030 Study: A Path to Revolutionary Computational Aerosciences," *Technical Report, NASA/CR-2014-218178, NF1676L-18332*, 2014.

[6] Williams, O., Samuell, M., Sarwas, E. S., Robbins, M., and Ferrante, A., "Experimental Study of a CFD Validation Test Case for Turbulent Separated Flows," *AIAA Scitech 2020 Forum*, 2020, pp. 1–19. https://doi.org/10.2514/6.2020-0092.

[7] Agrawal, R., Whitmore, M. P., Griffin, K. P., Bose, S. T., and Moin, P., "Non-Boussinesq subgrid-scale model with dynamic tensorial coefficients," *Phys. Rev. Fluids*, Vol. 7, 2022, p. 074602. https://doi.org/10.1103/PhysRevFluids.7.074602.

[8] Driver, D. M., and Seegmiller, H. L., "Features of a reattaching turbulent shear layer in divergent channelflow," *AIAA J.*, Vol. 23, No. 2, 1985, pp. 163–171. https://doi.org/10.2514/3.8890.

[9] Cho, M., Lozano-Durán, A., Moin, P., and Park, G. I., "Wall-Modeled Large-Eddy Simulation of Turbulent Boundary Layers with Mean-Flow Three-Dimensionality," *AIAA J.*, Vol. 59, No. 5, 2021, pp. 1707–1717. https://doi.org/10.2514/1.J059861.

[10] Iyer, P. S., and Malik, M. R., "Wall-modeled LES of flow over a Gaussian bump," *AIAA Scitech 2021 Forum*, 2021, pp. 1–18. https://doi.org/10.2514/6.2021-1438.

[11] Iyer, P. S., and Malik, M. R., "Wall-modeled LES of the Three-dimensional Speed Bump Experiment," *AIAA SCITECH 2023 Forum*, 2023, pp. 1–17. https://doi.org/10.2514/6.2023-0253.

[12] Lozano-Durán, A., and Bae, H. J., "Error scaling of large-eddy simulation in the outer region of wall-bounded turbulence," *J. Comp. Phys.*, Vol. 392, 2019, pp. 532–555.

[13] Lozano-Durán, A., Bose, S. T., and Moin, P., "Performance of Wall-Modeled LES with Boundary-Layer-Conforming Grids for External Aerodynamics," *AIAA Journal*, Vol. 60, No. 2, 2022, pp. 747–766. https://doi.org/10.2514/1.J061041.

[14] Lund, T. S., and Novikov, E. A., "Parameterization of subgrid-scale stress by the velocity gradient tensor," *Annual Research Briefs, 1992*, 1993.

[15] Vreman, A. W., "An eddy-viscosity subgrid-scale model for turbulent shear flow: Algebraic theory and applications," *Phys. Fluids*, Vol. 16, No. 10, 2004, pp. 3670–3681. https://doi.org/10.1063/1.1785131.

[16] Nocedal, J., and Wright, S. J., *Numerical optimization*, Springer, 1999.

[17] Pelikan, M., *Bayesian Optimization Algorithm*, Springer Berlin Heidelberg, Berlin, Heidelberg, 2005, Chap. 8, pp. 31–48. https://doi.org/10.1007/978-3-540-32373-0_3.

[18] N., F., "Bayesian Optimization: Open source constrained global optimization tool for Python," , 2014–. URL https://github.com/fmfn/BayesianOptimization.

[19] Del Alamo, J. C., Jiménez, J., Zandonade, P., and Moser, R. D., "Scaling of the energy spectra of turbulent channels," *J. Fluid Mech.*, Vol. 500, 2004, pp. 135–144. https://doi.org/10.1017/S002211200300733X.

[20] Hoyas, S., and Jiménez, J., "Scaling of the velocity fluctuations in turbulent channels up to $Re_\tau = 2003$," *Phys. Fluids*, Vol. 18, No. 1, 2006, p. 011702. https://doi.org/10.1063/1.2162185.

[21] Lozano-Durán, A., and Jiménez, J., "Effect of the computational domain on direct simulations of turbulent channels up to $Re_\tau = 4200$," *Phys. Fluids*, Vol. 26, No. 1, 2014, p. 011702. https://doi.org/10.1063/1.4862918.

[22] Hoyas, S., Oberlack, M., Alcántara-Ávila, F., Kraheberger, S. V., and Laux, J., "Wall turbulence at high friction Reynolds numbers," *Phys. Rev. Fluids*, Vol. 7, 2022, p. 014602. https://doi.org/10.1103/PhysRevFluids.7.014602.

[23] Gray, P. D., Gluzman, I., Thomas, F. O., and Corke, T. C., "Experimental Characterization of Smooth Body Flow Separation Over Wall-Mounted Gaussian Bump," *AIAA Scitech 2022 Forum*, 2022, pp. 1–23. https://doi.org/10.2514/6.2022-1209.

[24] Germano, M., Piomelli, U., Moin, P., and Cabot, W. H., "A dynamic subgrid-scale eddy viscosity model," *Physics of Fluids A: Fluid Dynamics*, Vol. 3, No. 7, 1991, pp. 1760–1765. https://doi.org/10.1063/1.857955.

[25] Larsson, J., Kawai, S., Bodart, J., and Bermejo-Moreno, I., "Large eddy simulation with modeled wall-stress: recent progress and future directions," *Mech. Eng. Rev.*, Vol. 3, No. 1, 2016, pp. 15–00418. https://doi.org/doi.org/10.1299/mer.15-00418.

[26] Fu, L., Karp, M., Bose, S. T., Moin, P., and Urzay, J., "Shock-induced heating and transition to turbulence in a hypersonic boundary layer," *J. Fluid Mech.*, Vol. 909, 2021, p. A8. https://doi.org/10.1017/jfm.2020.935.